photonics

MDPI

Article

Compact Gas Sensor Using Silicon-on-Insulator Loop-Terminated Mach–Zehnder Interferometer

Raghi S. El Shamy [1,2], Mohamed A. Swillam [1], Mohamed M. ElRayany [1], Alaa Sultan [1] and Xun Li [2,*]

[1] Department of Physics, School of Science and Engineering, The American University in Cairo, New Cairo 11835, Egypt; elshamyr@mcmaster.ca (R.S.E.S.); m.swillam@aucegypt.edu (M.A.S.); mohamedmansour@aucegypt.edu (M.M.E.); alaasultan@aucegypt.edu (A.S.)

[2] Department of Electrical and Computer Engineering, Faculty of Engineering, McMaster University, Hamilton, ON L8S 4L8, Canada

* Correspondence: lixun@mcmaster.ca; Tel.: +1-905-525-9140 (ext. 27698)

Abstract: In this paper, we propose a compact optical gas sensor based on the widespread silicon-on-insulator (SOI) technology, operating in the near-infrared (NIR) region around the 1.55 μm wavelength. The sensor employs a loop-terminated Mach–Zehnder interferometer (LT-MZI) with a slot waveguide and a strip waveguide for the sensing arm and the reference arm, respectively. For the same arm length, the LT-MZI can achieve a detection limit two times lower than that of the conventional MZI. Different sensor components were designed, and the optimum dimensions were obtained using finite-difference eigenmode (FDE) and finite-difference time-domain (FDTD) solvers. With a sensing arm length of only 150 μm, our sensor achieves a device sensitivity of 1070 nm/RIU and a figure-of-merit (FOM) as high as 280.8 RIU^{-1} at the 1.55 μm wavelength. Higher values of FOM can be attained by employing a longer sensing arm. The whole sensor is subjected to air cladding; thus, there is no need for oxide deposition and a further lithography step for sensing-area patterning. The sensor is well suited for low-cost fabrication and large-scale production. Finally, the same LT-MZI device with strip and slot arms but with oxide cladding was fabricated and characterized. The measurements were in good agreement with the electromagnetic (EM) simulation results, ensuring the reliability of our proposed design.

Keywords: gas sensing; silicon-on-insulator; Mach-Zehnder interferometer

Citation: El Shamy, R.S.; Swillam, M.A.; ElRayany, M.M.; Sultan, A.; Li, X. Compact Gas Sensor Using Silicon-on-Insulator Loop-Terminated Mach–Zehnder Interferometer. *Photonics* **2022**, *9*, 8. https://doi.org/10.3390/photonics9010008

Received: 8 December 2021
Accepted: 23 December 2021
Published: 27 December 2021

1. Introduction

Gas sensing is rapidly growing in importance due to its essential role in various fields and for a wide range of applications such as the detection of hazardous and toxic gases, industrial inspection, and environmental monitoring [1]. Several optical gas sensors have been developed over the years, owing to their high sensitivity, stability, wide dynamic range, fast response time, and multiplexing capabilities [1–5]. The demand for integrated on-chip photonics gas sensors is rising and is expected to increase further. Miniaturizing the footprint of these sensors using a complementary metal-oxide semiconductor (CMOS)-compatible technology is of great importance, to enable their integration with other optical and electrical functions, allowing compact devices to be produced on a mass scale using low-cost fabrication [6,7]. Co-integration with wireless communication systems so that toxic and flammable gases can be detected at safe distances is one example. The well-established silicon-on-insulator (SOI) technology has contributed to rapid and substantial progress in integrated photonics [8]. The SOI platform allows for submicron waveguide dimensions and hence, dense integration, owing to the high refractive index contrast between the silicon and the silicon dioxide. Another important advantage of this platform is its compatibility with CMOS technology.

Refractive index (RI) sensing, which detects the real part of the refractive index n, has been drawing increasing interest for its ability to directly detect unlabeled biomolecules

and because it has high sensitivity to small changes in the cover medium [9]. In this technique, the mode effective index n_{eff} of the sensing waveguide changes in accordance with a change in the refractive index of the medium n_{med}. Increasing the percentage of the mode field that passes through the sensing medium will increase the change in n_{eff}, hence resulting in higher sensitivity. The percentage of the mode field depends on the waveguide shape, its refractive indices, and its dimensions [10–13]. A slot waveguide has the capability of strongly confining and guiding light in nanoscale voids (low RI) between two high-index regions [13,14]. As a result, slot waveguides allow for higher field interaction with the analyte compared to other waveguides. Therefore, compact and highly sensitive sensors are realized. A myriad of configurations for integrated RI sensing have been reported, which can be classified mainly into interferometers [15–19] and microcavities [20–23]. Sensors based on microcavities are compact; however, they suffer from high sensitivity to any noise such as temperature fluctuations. On the other hand, interferometers, while less sensitive to such fluctuations, need a large footprint to achieve high performance. Plasmonic sensors based on surface plasmon–polariton (SPP) waves, which propagate along a metal surface, have also been proposed [24–29]. Such sensors can achieve large wavelength sensitivities due to the high light–matter interaction that can be obtained using a plasmonic waveguide, especially a plasmonic slot. However, the high losses accompanying the plasmonic modes result in poor resonances, which limits the overall sensor performance. In addition, plasmonic structures employ gold and silver, which are not standard CMOS-compatible materials.

It is important to note that RI sensors are not selective, i.e., they cannot determine the type of gas present in the medium. Such sensors can only be used in a medium where there is a single gas type. However, various materials have been used as a layer in optical sensors for selective gas sensing. Metal oxides have been widely investigated and utilized for selective detection, especially zinc oxide ZnO [30–35]. Thin layers, nanostructures, and doped metal oxides have all been employed. For instance, selective detection of NO_2, CO, and CH_4 was achieved using ZnO [32–34]. In addition, tungsten oxide WO_3 was used for selective H_2 detection [35]. Evanescent field absorption gas sensors, which detect the imaginary part of the refractive index k, can be selective by working around the absorption fingerprint of the gas [36–40]. However, these fingerprints are in the mid-infrared region where the photonic platforms are not as mature as in the near infrared. While absorption peaks are still present for some functional groups in the near infrared they are weak; hence, significantly large interaction lengths are needed.

In this paper, we propose a highly compact RI gas sensor using an SOI loop-terminated Mach–Zehnder interferometer (LT-MZI) and utilizing a slot waveguide in the sensing arm. In LT-MZI, the conventional MZI is cascaded with a Sagnac loop [41] at its end, which reduces the interferometer length by a factor of two. Implementing the sensor on the CMOS-compatible SOI technology allows for mass-scale low-cost fabrication of the sensor in addition to its integration with other optical and electrical components on the same chip. This study is an exhaustive extension of our previously published work [42].

In [43], the same structure is proposed for RI sensing but using optical fibers. In this study, the authors achieved a sensitivity as high as 10,000 nm/RIU with an 11 mm arm length. In [44], the structure is used as a tunable comb filter through phase modulating the Sagnac loop exhibiting ultra-fast wavelength tuning, also based on fibers. The authors in [45] implemented a similar structure as they utilized two Sagnac-loop reflectors to form a Fabry–Perot resonator for a bandwidth tunable filter using an SOI strip waveguide, achieving a tuning efficiency of 0.019 nm/mW. Furthermore, in [46], two loop mirrors are used to implement a Michelson interferometer modulator with a low $V_\pi \times L$ of 0.72 V-cm and a 500 μm phase-shifter length, again with an SOI strip waveguide.

Finite-difference eigenmode (FDE) [47] and finite-difference time-domain (FDTD) solvers [48] were used to design, optimize, and determine the performance of our LT-MZI gas sensor in the near-infrared (NIR) region. The results showed that our sensor can

achieve high performance with a small footprint. Finally, the same structure, but with oxide cladding rather than air, was fabricated and experimentally characterized.

2. Sensor Design

2.1. LT-MZI Structure and Analysis

The full structure of our LT-MZI gas sensor and its principle of operation are shown in Figure 1. The structure is based on the standard SOI technology with a 220 nm silicon device layer working at the 1.55 µm wavelength, with the whole sensor subjected to air cladding. A slot waveguide was used as the sensing arm to maximize the interaction with the gaseous medium. On the other hand, a wide strip waveguide was used as the reference arm, as well as for the other parts of the sensor, so that there was minimal interaction with the sensing medium. Two identical directional couplers (DCs) were designed to split/combine the incident light beam evenly between the two MZI arms. At the end, a Sagnac loop was used to reflect back the electromagnetic (EM) waves from the second DC outputs to the interferometer arms, and then to the output from the first DC, as shown in Figure 1b. This doubles the optical path length, giving it twice the physical length compared to the conventional MZI.

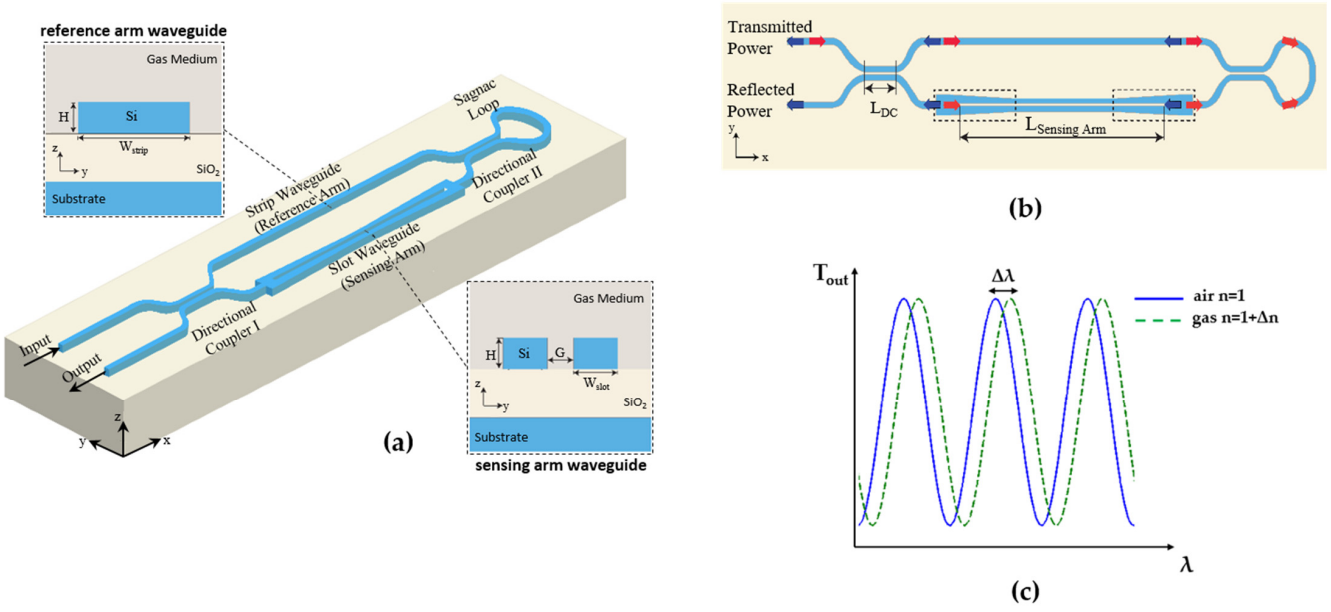

Figure 1. (**a**) Three-dimensional schematic of the LT-MZI gas sensor; insets: cross sections of the strip (reference arm) and slot (sensing arm) waveguides; (**b**) top view of the LT-MZI gas sensor showing the paths for the light beams with red and blue arrows, while marking the mode converters with a dotted-line box; (**c**) schematic of a typical LT-MZI interferometer transmission and the shift in the spectrum that occurs due to gas presence.

The transmission of the LT-MZI and the conventional MZI with 3 dB DCs can be derived as follows:

$$T_{LT-MZI} = \cos^2\left(\frac{2\pi\Delta n_{eff}L}{\lambda}\right) \quad (1a)$$

$$T_{MZI} = \cos^2\left(\frac{\pi\Delta n_{eff}L}{\lambda}\right) \quad (1b)$$

where $\Delta n_{eff} = n_{eff,sens} - n_{eff,ref}$, and $n_{eff,sens}$ and $n_{eff,ref}$ are the mode effective indices of the sensing arm and the reference arm, respectively. L is the length of the interferometer arms

and λ is the wavelength. From this, we can derive the wavelength sensitivity S, the full width at half maximum (FWHM), and the free spectral range (FSR), as follows:

$$S_{LT-MZI} = S_{MZI} = \frac{d\lambda_{res}}{dn_{med}} = \frac{\lambda_{res}}{\Delta n_{eff}}\left(S_{wg,sens} - S_{wg,ref}\right) \quad (2)$$

$$FWHM = \frac{FSR}{\pi} \quad (3)$$

$$\text{with } FSR_{LT-MZI} = \frac{\lambda^2}{2\Delta n_{ef} L} \quad (4a)$$

$$\text{and } FSR_{MZI} = \frac{\lambda^2}{\Delta n_{ef} L} \quad (4b)$$

$$\text{where } S_{wg} = \frac{dn_{eff}}{dn_{med}} \quad (5)$$

is the waveguide sensitivity.

Note that a sensor with high sensitivity is not enough for good detection, as the FWHM of the sensor should also be minimized. Thus, a figure of merit (FOM) is defined for such sensors as the ratio between the wavelength sensitivity S and the FWHM. The FOM determines the intrinsic detection limit iDL [49] of an RI sensor, i.e., the minimum detectable refractive index change, as follows:

$$FOM = \frac{1}{iDL} = \frac{S}{FWHM} \quad (6)$$

Hence, using Equation (2) through Equations (4a) and (4b) we have:

$$FOM_{LT-MZI} = 2FOM_{MZI} = \frac{2\pi\left(S_{wg,sens} - S_{wg,ref}\right)L}{\lambda} \quad (7)$$

As can be seen, for the same interferometer arm length, the LT-MZI exhibits twice the FOM of the conventional MZI, and hence an enhanced detection limit.

2.2. Components Design

A DC with a gap G_{DC} of 100 nm and a length L_{DC} of 12.1 μm was designed using 3D-FDTD to work as a 3 dB coupler at 1.55 μm. Next, we optimized the slot waveguide with a 100 nm slot gap width G_{slot} such that we maximized the waveguide sensitivity S_{wg}. S_{wg} was determined at λ = 1.55 μm using the FDE solver and Equation (5). A change in the air cladding medium index Δn_{med} of 0.001 was introduced and the corresponding change in the mode effective index Δn_{eff} was calculated using the FDE solver from which the S_{wg} value was determined with Equation (5). Figure 2a shows the S_{wg} of the quasi-transverse electric (TE) mode for both the slot and strip waveguide versus the silicon waveguide width. The results show that there is an optimum width for both waveguides that maximizes S_{wg}. This is expected because, at small silicon widths a significant part of the evanescent field is confined in the substrate, resulting in a low S_{wg}, while for large silicon widths most of the field will be confined inside the silicon. Hence, there is an optimum width where the field in the cladding is maximized. According to the results shown in Figure 2a, we chose the silicon width of the slot waveguide to be W_{slot} = 270 nm, which gave the highest S_{wg} value of 0.7. On the other hand, wide strip waveguides allow for better confinement, and hence lower sensitivity, and lower propagation and bend loss. Therefore, we chose W_{strip} = 500 nm, which was the largest possible waveguide width, while maintaining single-mode operation, resulting in an S_{wg} as low as 0.1. For this design, there is no need for capped oxide deposition and subsequent lithography and etching of a sensing area.

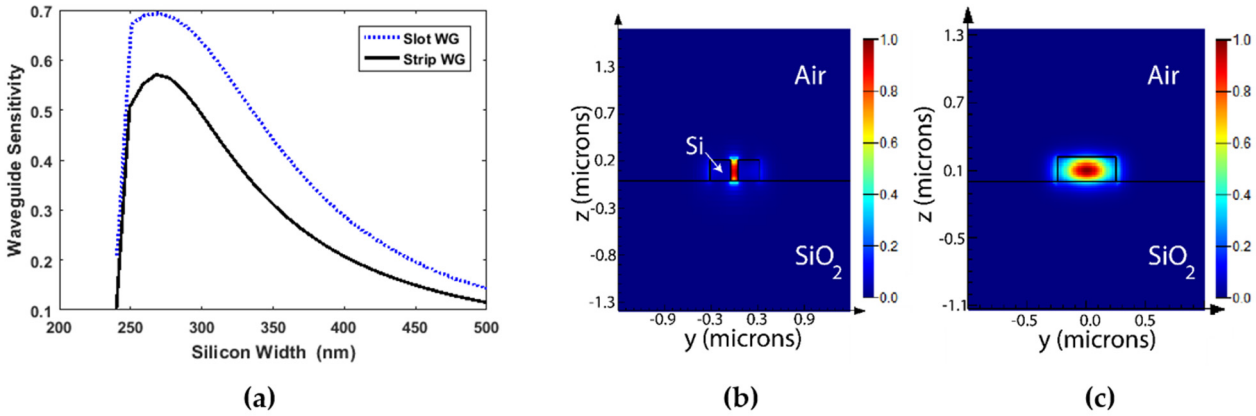

Figure 2. (**a**) Waveguide sensitivity S_{wg} of the quasi-TE mode of both the strip and the slot waveguides as a function of the silicon widths at λ = 1.55 μm. The fundamental quasi-TE mode of: (**b**) the slot waveguide with W_{slot} = 270 nm and (**c**) the strip waveguide with W_{strip} = 500 nm.

The mode mismatch between the slot and strip waveguides (see Figure 2b,c) makes the coupling challenging. To tackle this problem, a mode converter was designed. Various designs have been realized for such a converter [50–53]. The work in [53] was adapted for our LT-MZI gas sensor. A conversion efficiency higher than 95% for both the quasi-TE and quasi-TM modes was experimentally demonstrated in this study. The converter also works over a wide bandwidth range from 1.475 μm to 1.6 μm, where our sensor is operating, and it shows high tolerance to fabrication errors. The mode converter is composed of two sections: a multi-mode interferometer (MMI) and a slot taper (see Figure 3a). As illustrated in the field profile of the converter shown in Figure 3b, the MMI is used to split the input light into two identical beams, while the taper section gradually pushes the field to the slot. The dimensions of the mode converter as indicated in Figure 3a were optimized using 3D-FDTD simulations, to reduce the insertion loss (IL) and to improve its overall performance. The IL is calculated as follows:

$$IL = 10\log(T_{out}) \quad (8)$$

where $T_{out} = P_{out}/P_{in}$ is the output transmission, P_{out} is the output power transmitted through the slot waveguide quasi-TE mode, and P_{in} is the input power launched to the strip waveguide fundamental quasi-TE mode. T_{out} is easily calculated using the power monitor of the FDTD solver.

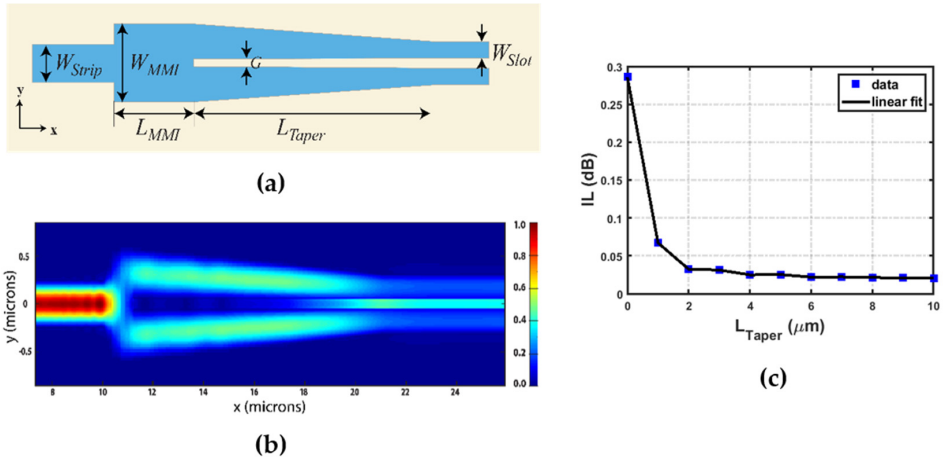

Figure 3. (**a**) Schematic of the mode converter; (**b**) quasi-TE-mode profile of the mode converter as depicted from FDTD solver; (**c**) the insertion loss of the mode converter as a function of the length of its taper section at λ = 1.55 μm.

The simulation results show that the IL is highly dependent on the taper length, L_{Taper}. As demonstrated in Figure 3c, we found that for an IL lower than 0.05 dB, the length of the taper section must be greater than 3 µm. Based on this conclusion, the dimensions of the optimized mode converter were designed to be W_{MMI} = 1.1 µm and L_{MMI} = 1.2 µm, with L_{Taper} equal to 5 µm. Finally, to ensure negligible losses, the Sagnac-loop bend radius R, was 5 µm [54]. It is important to note that perfectly-matched-layer (PML) boundary conditions and a minimum of 10 meshes in every dimension in the object's cross section were used in all simulations, with both the FDE and FDTD solvers. In addition, for the FDTD simulations, a spectral window of 100 nm from 1.5 µm to 1.6 µm was simulated.

3. LT-MZI Sensor Simulation Results

To determine the performance of the whole sensor, i.e., obtain the LT-MZI output transmission spectrum, the Lumerical INTERCONNECT [55] photonic circuit simulator was used. In this tool, the FDTD simulation results of the different components are used to obtain the overall LT-MZI sensor response via the scattering matrix method. This allows for fast and accurate simulation of the whole LT-MZI sensor for different lengths and different medium indices. Note that the refractive index of gases is typically very close to 1 with $\Delta n = n_{gas} - 1$ less than 10^{-3}. However, this refractive index can vary significantly depending on the pressure, reaching a value of Δn of the order of 10^{-3} [56]. Therefore, we varied the cladding medium index over a wide range from 1 to 1.009. In Figure 4a, the output transmission spectra of our sensor with L = 50 µm for different surrounding medium indices are shown. The effective index dispersion n_{eff} (λ) from 1.5 µm to 1.6 µm was calculated for the strip and slot waveguide modes for different cladding indices using the FDE solver, and these were then used in INTERCONNECT to determine the corresponding output transmission spectrum.

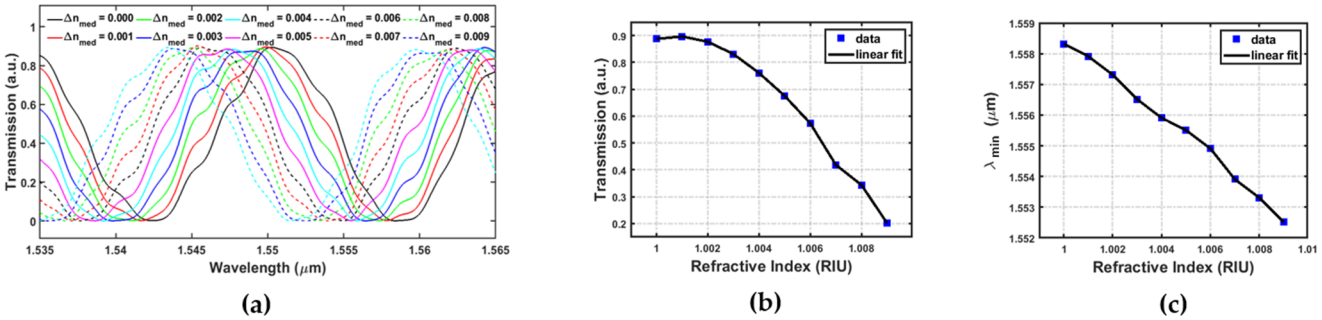

Figure 4. (**a**) The output transmission spectra of the LT-MZI sensor with a length L of 50 µm at different refractive indices ranging from 1.000 to 1.009; (**b**) LT-MZI sensor transmission versus the medium's refractive index around λ = 1.55 µm with L = 50 µm; (**c**) LT-MZI sensor minimum wavelength versus the medium refractive index with L = 50 µm.

There are two main sensing schemes for the determination of the refractive index of the sensing medium: intensity interrogation and wavelength interrogation. In the intensity interrogation scheme, the medium's refractive index is determined by the change in the output intensity (transmission) at a specific wavelength (see Figure 4a). Figure 4b depicts the change in the output transmission at λ = 1.55 µm due to the change in the refractive index of the medium for our LT-MZI sensor with L = 50 µm. In the wavelength interrogation scheme, the medium's refractive index is determined by the shift in the resonance wavelength $d\lambda_{res}$ (see Figure 4a). Figure 4c shows the shift in the resonance wavelength due to the change in the refractive index of the medium for our LT-MZI sensor with L = 50 µm.

Next, the FOM of our LT-MZI sensor design was calculated from the transmission spectra obtained by the INTERCONNECT simulations and Equation (6), where the wavelength sensitivity S and the FWHM were first calculated. In Figure 5a, the dependence of the FOM on the medium index change Δn_{med} is determined. It can be seen that a lower

Δn_{med} results in a higher FOM; hence, our design is suitable for gas sensing where the refractive index is very close to 1. In addition, as expected from Equation (7), increasing the interferometer's arm length increases the FOM in an almost linear manner, as shown in Figure 5b, reaching 280.8 RIU^{-1} at L = 150 μm and a wavelength of around λ = 1.55 μm. The results also show that for L = 150 μm, the wavelength sensitivity reaches 1070 nm/RIU for λ = 1.55 μm. Finally, we point out that the design of the LT-MZI gas sensor can be applied using even longer sensing arms than the ones used in this study, to achieve higher values of sensitivity and the FOM.

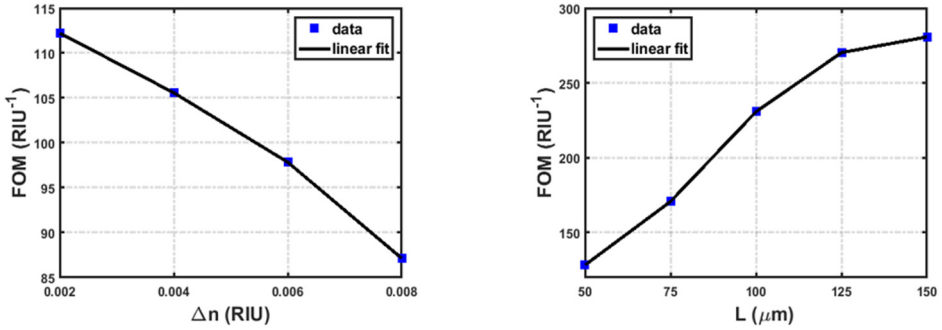

Figure 5. (**a**) LT-MZI sensor FOM calculated at different medium index changes (Δn) with L = 50 μm; (**b**) LT-MZI sensor FOM versus interferometer arm length.

4. Passive LT-MZI Structure Experimental Characterization

The same LT-MZI structure as in Figure 1 but with oxide cladding rather than air, denoted the passive LT-MZI, was fabricated and experimentally characterized. However, no gas sensing measurement could be performed using this device as it is not subjected to air, and accordingly the device's sensing performance cannot be determined. Our goal in this fabrication run was to ensure the reliability of our proposed LT-MZI design. This was achieved by comparing the measured response of the fabricated devices (LT-MZI capped with oxide cladding) with their corresponding numerical simulations. Here, two LT-MZIs capped with oxide with arm lengths L of 50 μm and 150 μm were simulated, fabricated, and characterized.

The fabrication of the structures was achieved using a multi-project wafer (MPW) on a 200 mm SOI wafer with a 220 nm silicon device layer at the University of Washington Nanofabrication Facility [57], using electron beam lithography (EBL). Figure 6a shows the waveguide fabrication steps. EBL with a negative resist and inductively coupled plasma (ICP) etching (using chlorine gas) were used for silicon patterning. Then, plasma-enhanced chemical vapor deposition (PECVD) was used to deposit around 2 μm of oxide cladding. The device characterization was performed by the MiNa group at the University of British Columbia [58] and at Maple Leaf Photonics [59]. The measurement setup, shown in Figure 6b, included a tunable laser from 1500 nm to 1600 nm wavelength, a polarization-maintaining fiber array with four fibers for the i/o optical signal, and a multi-channel photodetector. Grating couplers on each device on the chip were used to couple the optical signal from/to the fiber array. The chip was placed on an automated stage with 2D movement. The stage was linked to a computer with software that automated the measurements by controlling the movement of the stage using the GDS file of the chip to trace and measure the different optical devices on the chip. A temperature controller was also used to adjust the temperature of the stage. Using this setup, the transmission spectra of the different devices could be measured in a fast and accurate manner.

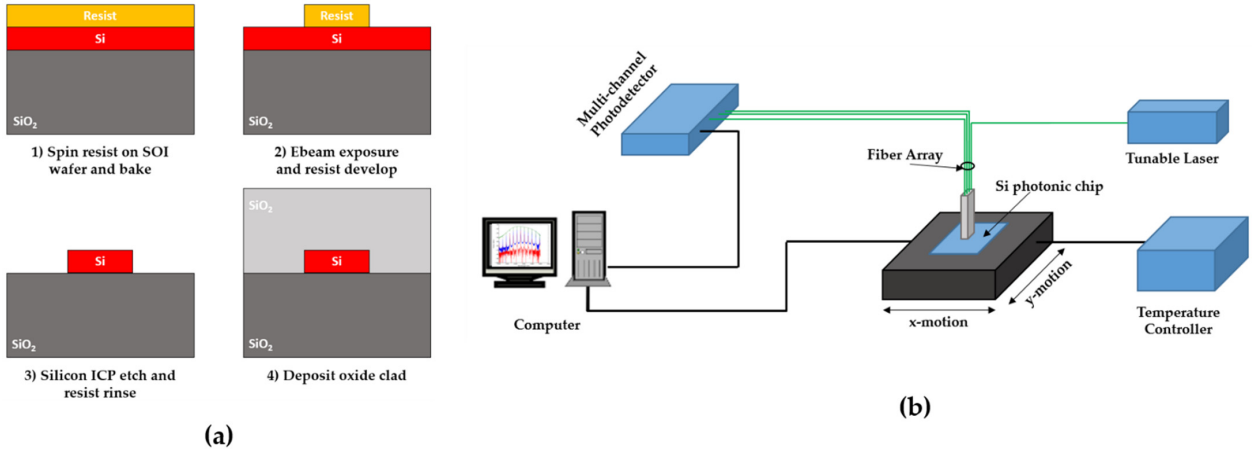

Figure 6. (**a**) Silicon waveguide fabrication steps using EBL; (**b**) schematic of the measurement setup.

The layout of the fabricated LT-MZI and SEM images of its various components are shown in Figure 7a. The measured transmission spectra of the LT-MZIs with L = 50 µm and L = 150 µm are shown in Figure 7b,c, respectively, along with the corresponding INTERCONNECT simulation results. It can be seen that there is a good match in the device response between the simulation and the measurement results. The FSR calculated from the measurements was 11.24 nm and 4.19 nm with 1.1% and 2.18% deviation from the simulation results for the 50 µm and 150 µm devices, respectively. These results further ensured that the numerical simulation results we obtained previously could be trusted.

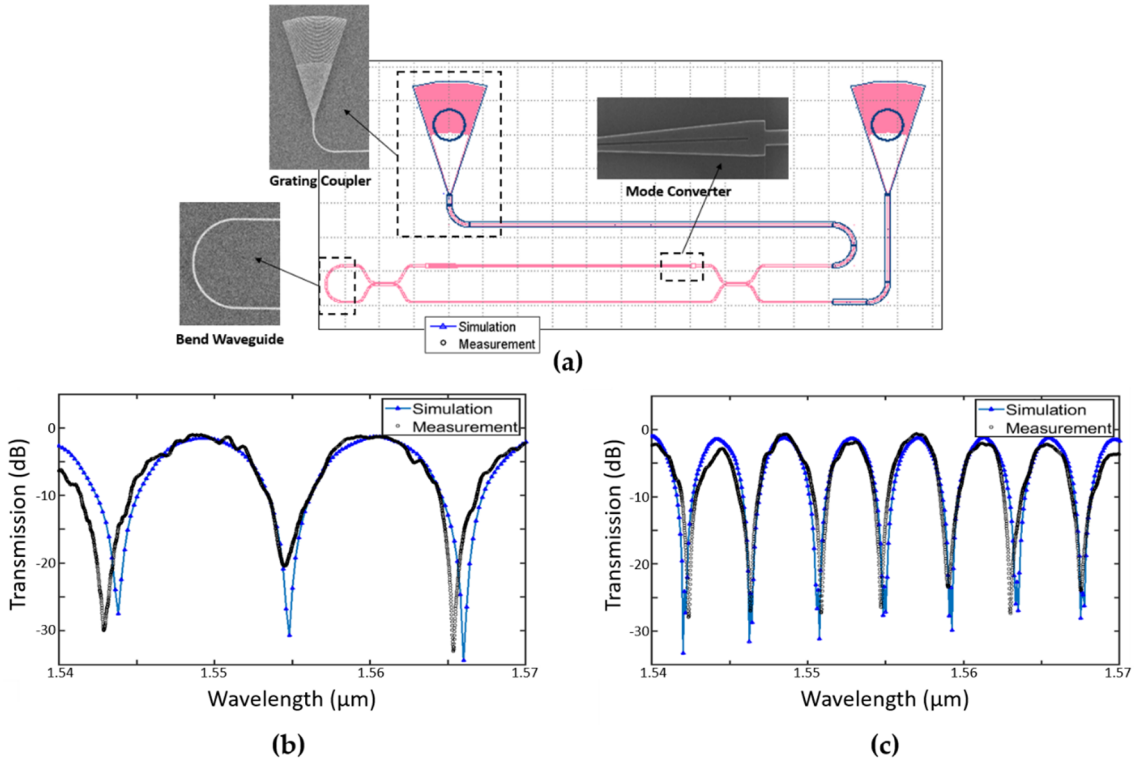

Figure 7. (**a**) Layout of the fabricated LT-MZI with L = 50 µm; insets showing the SEM images of various components. Simulated and measured transmission spectra of the LT-MZI structure with oxide cladding: (**b**) L = 50 µm; (**c**) L = 150 µm.

5. Conclusions

We presented a compact SOI-based RI gas sensor using a MZI interferometer cascaded with a Sagnac loop forming a loop-terminated MZI. The LT-MZI sensor achieved the

same performance as a conventional MZI with only half its length. A slot waveguide was designed to achieve maximum waveguide sensitivity and, consequently, to maximize the overall device sensitivity. The different sensor components were designed and optimized using FDE and FDTD solvers. A strip-to-slot waveguide mode converter was optimized to minimize the insertion loss between the two waveguides. The simulation results based on the FDTD solver showed that our design could achieve a high sensitivity of 1070 nm/RIU and a high FOM of 280.8 RIU^{-1} using a length of only 150 µm, with higher values of FOM possible at a longer arm lengths. The same LT-MZI structure but with oxide cladding was experimentally characterized, showing a good agreement with the theoretical simulations. Thus, our proposed LT-MZI gas sensor is a good candidate for efficient and compact on-chip sensors with low-cost and mass-scale fabrication, due to the CMOS-compatible SOI platform.

Author Contributions: Conceptualization, M.A.S. and R.S.E.S.; methodology, M.A.S. and R.S.E.S.; software, M.M.E., R.S.E.S. and A.S.; validation, M.M.E., R.S.E.S. and M.A.S.; formal analysis, M.M.E. and R.S.E.S.; investigation, R.S.E.S. and M.A.S.; resources, M.A.S.; data curation, M.M.E. and R.S.E.S.; writing—original draft preparation, M.M.E. and R.S.E.S.; writing—review and editing, R.S.E.S., M.A.S. and X.L.; visualization M.M.E., R.S.E.S. and A.S.; supervision, M.A.S. and X.L.; project administration, M.A.S. and X.L.; funding acquisition, M.A.S. All authors have read and agreed to the published version of the manuscript.

Funding: This research was funded in part by ITIDA-ITAC, grant number CFP198 and also by the internal research support from the American University in Cairo.

Conflicts of Interest: The authors declare no conflict of interest. The funders had no role in the design of the study, in the collection, analyses, or interpretation of data, in the writing of the manuscript, or in the decision to publish the results.

References

1. Hodgkinson, J.; Tatam, R.P. Optical gas sensing: A review. *Meas. Sci. Technol.* **2012**, *24*, 012004. [CrossRef]
2. Yebo, N.A.; Lommens, P.; Hens, Z.; Baets, R. An integrated optic ethanol vapor sensor based on a silicon-on-insulator microring resonator coated with a porous ZnO film. *Opt. Express* **2010**, *18*, 11859–11866. [CrossRef]
3. Dullo, F.T.; Lindecrantz, S.; Jágerská, J.; Hansen, J.H.; Engqvist, S.O.M.; Solbø, S.; Hellesø, O.G. Sensitive on-chip methane detection with a cryptophane-A cladded Mach-Zehnder interferometer. *Opt. Express* **2015**, *23*, 31564–31573. [CrossRef]
4. Mi, G.; Horvath, C.; Van Silicon, V. Photonic dual-gas sensor for H_2 and CO_2 detection. *Opt. Express* **2017**, *25*, 16250. [CrossRef] [PubMed]
5. Gervais, A.; Jean, P.; Shi, W.; LaRochelle, S. Design of Slow-Light Subwavelength Grating Waveguides for Enhanced On-Chip Methane Sensing by Absorption Spectroscopy. *IEEE J. Sel. Top. Quantum Electron.* **2018**, *25*, 1–8. [CrossRef]
6. Ghosh, S.; Dar, T.; Viphavakit, C.; Pan, C.; Kejalakshmy, N.; Rahman, B.M. Rahman, compact photonic SOI sensors. In *Computational Photonic Sensors*; Hameed, M., Obayya, S., Eds.; Springer: Cham, Switzerland, 2019; pp. 343–383.
7. Tsybeskov, L.; Lockwood, D.J.; Ichikawa, M. Silicon photonics: CMOS going optical [scanning the issue]. *Proc. IEEE* **2009**, *97*, 1161–1165. [CrossRef]
8. Bogaerts, W.; Selvaraja, S.K. Silicon-on-insulator (SOI) technology for photonic integrated circuits (PICs). In *Silicon-On-Insulator (SOI) Technology*; Woodhead Publishing: Sawston, UK, 2014; pp. 395–434. [CrossRef]
9. Fan, X.; White, I.M.; Shopova, S.I.; Zhu, H.; Suter, J.; Sun, Y. Sensitive optical biosensors for unlabeled targets: A review. *Anal. Chim. Acta* **2008**, *620*, 8–26. [CrossRef]
10. Parriaux, O.; Veldhuis, G. Normalized analysis for the sensitivity optimization of integrated optical evanescent-wave sensors. *J. Light. Technol.* **1998**, *16*, 573–582. [CrossRef]
11. Veldhuis, G.J.; Parriaux, O.; Hoekstra, H.J.; Lambeck, P.V. Lambeck Sensitivity enhancement in evanescent optical wave-guide sensors. *J. Lightwave Technol.* **2000**, *18*, 677–682. [CrossRef]
12. Densmore, A.; Post, E.; Xu, D.-X.; Waldron, P.; Janz, S.; Cheben, P.; Lapointe, J.; Delage, A.; Lamontagne, B.; Schmid, J.H. A Silicon-on-Insulator Photonic Wire Based Evanescent Field Sensor. *IEEE Photon-Technol. Lett.* **2006**, *18*, 2520–2522. [CrossRef]
13. Dell'Olio, F.; Passaro, V.M.N. Optical sensing by optimized silicon slot waveguides. *Opt. Express* **2007**, *15*, 4977–4993. [CrossRef] [PubMed]
14. Almeida, V.; Xu, Q.; Barrios, C.A.; Lipson, M. Guiding and confining light in void nanostructure. *Opt. Lett.* **2004**, *29*, 1209–1211. [CrossRef]
15. Prieto, F.; Sepúlveda, B.; Calle, A.; Llobera, A.; Domínguez, C.; Abad, A.; Montoya, A.; Lechuga, L.M. Lechuga an integrated optical interferometric nanodevice based on silicon technology for biosensor applications. *Nanotechnology* **2003**, *14*, 907–912. [CrossRef]

16. Tian, Z.; Yam, S.S.; Loock, H.P. Refractive index sensor based on an abrupt taper michelson interferometer in a single-mode fiber. *Opt. Lett.* **2008**, *33*, 1105–1107. [CrossRef] [PubMed]
17. Yang, R.; Yu, Y.-S.; Xue, Y.; Chen, C.; Chen, Q.-D.; Sun, H.-B. Single S-tapered fiber Mach–Zehnder interferometers. *Opt. Lett.* **2011**, *36*, 4482–4484. [CrossRef] [PubMed]
18. Gao, Y.; Gan, Q.; Xin, Z.; Cheng, X.; Bartoli, F.J. Plasmonic Mach–Zehnder Interferometer for Ultrasensitive On-Chip Biosensing. *ACS Nano* **2011**, *5*, 9836–9844. [CrossRef]
19. El Shamy, R.S.; Swillam, M.A.; Khalil, D.A. Mid infrared integrated MZI gas sensor using suspended silicon waveguide. *J. Lightwave Technol.* **2019**, *37*, 4394–4400. [CrossRef]
20. Barrios, C.A.; Gylfason, K.B.; Sánchez, B.; Griol, A.; Sohlström, H.; Holgado, M.; Casquel, R. Slot-waveguide biochemical sensor. *Opt. Lett.* **2007**, *32*, 3080–3082. [CrossRef]
21. Grist, S.M.; Schmidt, S.A.; Flueckiger, J.; Donzella, V.; Shi, W.; Fard, S.T.; Kirk, J.T.; Ratner, D.M.; Cheung, K.C.; Chrostowski, L. Silicon photonic micro-disk resonators for label-free biosensing. *Opt. Express* **2013**, *21*, 7994–8006. [CrossRef] [PubMed]
22. Robinson, J.T.; Chen, L.; Lipson, M. On-chip gas detection in silicon optical microcavities. *Opt. Express* **2008**, *16*, 4296–4301. [CrossRef]
23. Tsigaridas, G.N. A study on refractive index sensors based on optical micro-ring resonators. *Photon-Sens.* **2017**, *7*, 217–225. [CrossRef]
24. Xie, Y.; Huang, Y.; Che, H.; Zhao, W.; Xu, W.; Li, X.; Li, J. Theoretical investigation of a plasmonic sensor based on a metal–insulator–metal waveguide with a side-coupled nanodisk resonator. *J. Nanophotonics* **2015**, *9*, 93099. [CrossRef]
25. Xie, Y.Y.; Huang, Y.X.; Zhao, W.L.; Xu, W.H.; He, C. A novel plasmonic sensor based on metal–insulator–metal waveguide with side-coupled hexagonal cavity. *IEEE Photonics J.* **2015**, *7*, 1–12. [CrossRef]
26. El Shamy, R.S.; Khalil, D.; Swillam, M.A. Mid infrared optical gas sensor using plasmonic Mach-Zehnder interferometer. *Sci. Rep.* **2020**, *10*, 1293. [CrossRef]
27. Ayoub, A.B.; Ji, D.; Gan, Q.; Swillam, M.A. Silicon plasmonic integrated interferometer sensor for lab on chip applications. *Opt. Commun.* **2018**, *427*, 319–325. [CrossRef]
28. Ayoub, A.B.; Swillam, M.A. Swillam. Silicon plasmonics on-chip mid-IR gas sensor. *IEEE Photonics Technol. Lett.* **2018**, *30*, 931–934. [CrossRef]
29. Zaki, A.O.; Kirah, K.; Swillam, M.A. Integrated optical sensor using hybrid plasmonics for lab on chip applications. *J. Opt.* **2016**, *18*, 085803. [CrossRef]
30. Kanan, S.M.; El-Kadri, O.M.; Abu-Yousef, I.A.; Kanan, M.C. Semiconducting Metal Oxide Based Sensors for Selective Gas Pollutant Detection. *Sensors* **2009**, *9*, 8158–8196. [CrossRef] [PubMed]
31. Dimitrov, I.G.; Dikovska, A.O.; Atanasov, P.A.; Stoyanchov, T.R.; Vasilev, T. Al doped ZnO thin films for gas sensor application. *J. Phys. Conf. Ser.* **2008**, *113*, 012044. [CrossRef]
32. Pineda-Reyes, A.M.; Herrera-Rivera, M.R.; Rojas-Chávez, H.; Cruz-Martínez, H.; Medina, D.I. Recent advances in ZnO-based carbon monoxide sensors: Role of doping. *Sensors* **2021**, *21*, 4425. [CrossRef]
33. Allsop, T.; Kundrat, V.; Kalli, K.; Lee, G.B.; Neal, R.; Bond, P.; Shi, B.; Sullivan, J.; Culverhouse, P.; Webb, D.J. Methane detection scheme based upon the changing optical constants of a zinc oxide/platinum matrix created by a redox reaction and their effect upon surface plasmons. *Sens. Actuators B Chem.* **2018**, *255*, 843–853. [CrossRef]
34. Gaur, R.; Padhy, H.M.; Elayaperumal, M. Surface plasmon assisted toxic chemical NO_2 gas sensor by Au/ZnO functional thin films. *J. Sens. Sens. Syst.* **2021**, *10*, 163–169. [CrossRef]
35. Amrehn, S.; Wu, X.; Wagner, T. Tungsten oxide photonic crystals as optical transducer for gas sensing. *ACS Sens.* **2018**, *3*, 191–199. [CrossRef]
36. Butt, M.A.; Degtyarev, S.A.; Khonina, S.N.; Kazanskiy, N.L. An evanescent field absorption gas sensor at mid-IR 3.39 μm wavelength. *J. Mod. Opt.* **2017**, *64*, 1892–1897. [CrossRef]
37. Ranacher, C.; Consani, C.; Hedenig, U.; Grille, T.; Lavchiev, V.; Jakoby, B. A photonic silicon waveguide gas sensor using evanescent-wave absorption. In Proceedings of the 2016 IEEE Sensors, Orlando, FL, USA, 30 October–3 November 2016; pp. 1–3. [CrossRef]
38. Koompai, N.; Limsuwan, P.; Le Roux, X.; Vivien, L.; Marris-Morini, D.; Chaisakul, P. Analysis of Si_3N_4 waveguides for on-chip gas sensing by optical absorption within the mid-infrared region between 2.7 and 3.4 μm. *Results Phys.* **2020**, *16*, 102957. [CrossRef]
39. Gutierrez-Arroyo, A.; Baudet, E.; Bodiou, L.; Nazabal, V.; Rinnert, E.; Michel, K.; Bureau, B.; Colas, F.; Charrier, J. Theoretical study of an evanescent optical integrated sensor for multipurpose detection of gases and liquids in the Mid-Infrared. *Sens. Actuators B Chem.* **2017**, *242*, 842–848. [CrossRef]
40. Elsayed, M.Y.; Ismail, Y.; Swillam, M.A. Semiconductor plasmonic gas sensor using on-chip infrared spectroscopy. *Appl. Phys. A* **2017**, *123*, 113. [CrossRef]
41. Mortimore, D.B. Fiber loop reflectors. *J. Light. Technol.* **1988**, *6*, 1217–1224. [CrossRef]
42. El-Rayany, M.M.; El Shamy, R.S.; Swillam, M.A. A compact silicon-on-insulator gas sensor. In Proceedings of the Silicon Photonics XIV, International Society for Optics and Photonics, San Francisco, CA, USA, 4–6 February 2019; Volume 10923.
43. Han, C.; Ding, H.; Lv, F. Demonstration of a refractometric sensor based on an optical micro-fiber three-beam interferometer. *Sci. Rep.* **2014**, *4*, 7504. [CrossRef]

44. Guo, J.-J.; Yang, Y.; Peng, G.-D. Analysis of polarization-independent tunable optical comb filter by cascading MZI and phase modulating Sagnac loop. *Opt. Commun.* **2011**, *284*, 5144–5147. [CrossRef]
45. Jiang, X.; Wu, J.; Yang, Y.; Pan, T.; Mao, J.; Liu, B.; Liu, R.; Zhang, Y.; Qiu, C. Wavelength and bandwidth-tunable silicon comb filter based on Sagnac loop mirrors with Mach-Zehnder interferometer couplers. *Opt. Express* **2016**, *24*, 2183–2188. [CrossRef]
46. Patel, D.; Veerasubramanian, V.; Ghosh, S.; Samani, A.; Zhong, Q.; Plant, D.V. High-speed compact silicon photonic Michelson interferometric modulator. *Opt. Express* **2014**, *22*, 26788–26802. [CrossRef]
47. Optical Waveguide Design Software-Lumerical MODE Solutions Lumerical. Available online: https://www.lumerical.com/products/mode-solutions/ (accessed on 20 December 2021).
48. Nanophotonic FDTD Simulation Software-Lumerical FDTD Lumerical. Available online: https://www.lumerical.com/products/fdtd/ (accessed on 20 December 2021).
49. Yoshie, T.; Tang, L.; Su, S.Y. Optical microcavity: Sensing down to single molecules and atoms. *Sensors* **2011**, *11*, 1972–1991. [CrossRef]
50. Wang, Z.; Zhu, N.; Tang, Y.; Wosinski, L.; Dai, D.; He, S. Ultracompact low-loss coupler between strip and slot wave guides. *Opt. Lett.* **2009**, *34*, 1498–1500. [CrossRef]
51. Palmer, R.; Alloatti, L.; Korn, D.; Heni, W.; Schindler, P.C.; Bolten, J.; Karl, M.; Waldow, M.; Wahlbrink, T.; Freude, W.; et al. Low-Loss Silicon Strip-to-Slot Mode Converters. *IEEE Photon-J.* **2013**, *5*, 2200409. [CrossRef]
52. Zhang, H.; Zhang, J.; Chen, S.; Song, J.; Kee, J.S.; Yu, M.; Lo, G.-Q. CMOS-Compatible Fabrication of Silicon-Based Sub-100-nm Slot Waveguide with Efficient Channel-Slot Coupler. *IEEE Photon-Technol. Lett.* **2011**, *24*, 10–12. [CrossRef]
53. Deng, Q.; Yan, Q.; Liu, L.; Li, X.; Michel, J.; Zhou, Z. Robust polarization-insensitive strip-slot waveguide mode-converter based on symmetric multimode interference. *Opt. Express* **2016**, *24*, 7347–7355. [CrossRef] [PubMed]
54. Vlasov, Y.; McNab, S.J. Losses in single-mode silicon-on-insulator strip waveguides and bends. *Opt. Express* **2004**, *12*, 1622–1631. [CrossRef] [PubMed]
55. PIC Design and Simulation Software-Lumerical Interconnect Lumerical. Available online: https://www.lumerical.com/products/interconnect/ (accessed on 20 December 2021).
56. Sang, B.H.; Jeon, T.I. Pressure-dependent refractive indices of gases by THz time-domain spectroscopy. *Opt. Express* **2016**, *24*, 29040–29047. [CrossRef] [PubMed]
57. Equipment/Capabilities UW NNCI Washington Nanofabrication Facility Website. Available online: https://www.wnf.washington.edu/about/equipment/ (accessed on 20 December 2021).
58. Microsystems and Nanotechnology (MiNa) Group-The University of British Columbia Website. Available online: https://mina.ubc.ca/ (accessed on 20 December 2021).
59. Maple Leaf Photonics Website. Available online: http://mapleleafphotonics.com/ (accessed on 20 December 2021).